Soft Matter

PAPER

View Article Online
View Journal | View Issue

Cite this: *Soft Matter*, 2025, **21**, 7925

Controlling the local compliances of cruciform samples to probe equibiaxial failure

Majed N. Saadawi and Christopher W. Barney *

Multiaxial loading states are known to develop in common design structures such as corners, joints, and thin-walled shells. Despite the prevalence of multiaxial stress states in design, the characterization of multiaxial behavior in soft polymers and gels has lagged behind that for stiff materials where standards have been developed to perform such measurements. Given the lack of standardization, determining an appropriate geometry and method to probe the multiaxial mechanical response of soft materials falls under the purview of the individual researcher. Herein cruciform samples capable of quantifying the failure behavior of soft polymers under biaxial tension are designed. Using digital image correlation to quantify the local deformations, it is found that controlling the relative compliances of the legs to the center square is key to observing multiaxial failure. Further, controlling the transverse stiffness of the legs is found to significantly impact the uniformity of the deformation state that develops in the center square. Finally, the failure stresses measured in cruciform samples with varied corner geometry are found to be in reasonable agreement with independent measurements of the failure stress from uniaxial extension and equibiaxial inflation. These findings have strong implications for the design of structures where multiaxial stress states develop during regular use.

Received 23rd June 2025,
Accepted 24th September 2025

DOI: 10.1039/d5sm00644a

rsc.li/soft-matter-journal

Exploiting benchtop measurements to extract material behavior that translates to real world loadings is a foundational goal in the mechanics of materials. To do this, it is necessary to produce stress states that are analogous to the complex stress states that can arise during loading.[1–10] Despite the complex nature of these stress states, laboratory measurements are typically performed using simplified loadings that subject a standard geometry, such as that of the dogbone or compression disk, to a uniaxial stress state.[11,12] While these loadings are incredibly useful, their uniaxial nature inherently limits them when comparing to the multiaxial loadings that develop in structures such as joints, corners, and thin shells.[7,13] This limitation arises because the failure response of materials is well-documented to be sensitive to the applied stress state.[7,14–18] This means that it is necessary to measure the failure response of materials under multiaxial stress states in laboratory settings. A convenient means of accomplishing this is to perform biaxial tension in which the stresses in two directions are independently controlled. To perform biaxial tension, one must first select an appropriate geometry, such as that of the cruciform, to afford biaxial stress control.

While biaxial tension is a promising method to produce controlled multiaxial stress states, selecting an appropriate geometry to perform this technique is challenging for multiple reasons. First, unlike stiff materials,[19] soft materials can undergo large deformations before failing. These large deformations leave them vulnerable to developing potentially large variations in the local stress state during loading. This issue is most commonly addressed through direct visualization of the local deformations *via* digital image correlation (DIC).[20–25] Another challenge lies in the use of re-entrant corners in cruciform samples that can act as stress concentrators. While this problem can be managed through sample design, it is an inherent drawback of this geometry. Thus researchers hoping to perform biaxial tension to failure must carefully control the cruciform geometry to address the challenges above.

A sketch of a cruciform geometry, inspired by Donne *et al.*,[19] is shown in Fig. 1(a). The name cruciform derives from the cross-like nature of the sample and its shape is analogous to two dogbones oriented perpendicular to one another so that a biaxial stress state develops in the center square. Cruciforms have been commonly used for biaxial testing of stiff materials. Currently, no standards for cruciform samples have been developed with soft materials in mind.[26] While there is no standard, significant efforts have been made in the literature, especially amongst the biomaterials community, to develop cruciform geometries for soft tissues and gels.[20–25,27–45] Often work in this area prioritizes characterizing the constitutive response of soft solids and places lesser emphasis on quantifying the failure response. Given the diffuse nature of literature

School of Polymer Science and Polymer Engineering, The University of Akron, Akron, OH 44325-3909, USA. E-mail: barneyc@uakron.edu; Fax: +1 330 972 5290; Tel: +1 330 972 4297

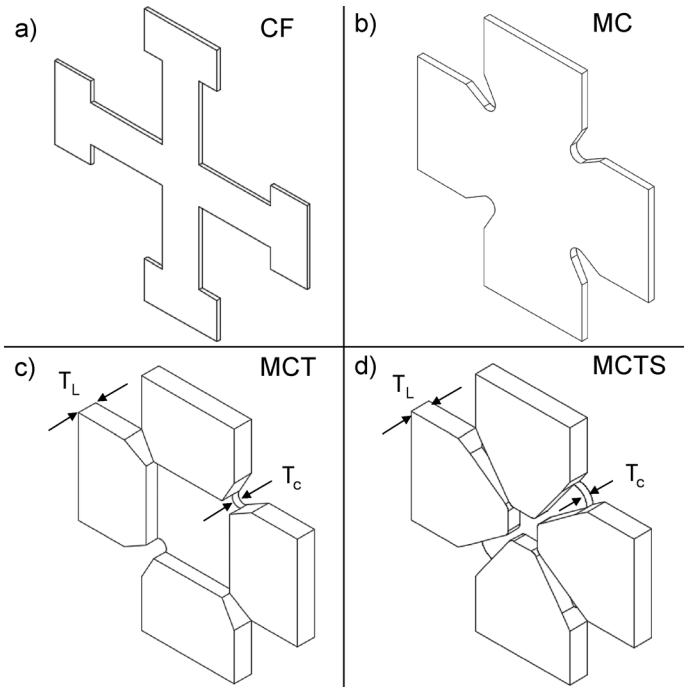

Fig. 1 Isometric view of the designs used in this investigation. (a) Cruciform (CF), (b) maltese cross (MC), (c) maltese cross with thickened legs (MCT) and (d) maltese cross thickened leg stress-distributed (MCTS). T_L and T_c refer to the leg and center square thicknesses, respectively. Molds are designed with T_L = 3 mm and T_c = 1 mm. Actual thickness values are recorded in Table S1.

in this area, those new to biaxial tension face ambiguous design criteria for creating cruciform samples. When facing nebulous constraints, researchers are left making systematic changes in specimen geometry until they are satisfied that it serves their purposes.[46] Based on these observations, we hypothesize that systematic control of the geometry in cruciform samples can be used to quantify the failure response of soft solids subjected to biaxial stress states.

This hypothesis is tested by systematically controlling the geometry of cruciform samples and benchmarking the failure performance against independent measurements. The cruciform samples are altered to control the axial compliance of the legs, transverse compliance of the legs, and the corner geometry. It is found that controlling all three of these aspects enables the characterization of failure in soft materials subjected to controlled biaxial stress states. These findings are important to advancing our understanding of physical phenomena such as the cavitation[47] and yielding[48] of soft solids.

1 Experimental

1.1 Materials

Samples were prepared from a Sylgard 184 kit that was sourced from Fisher Scientific and used as received. The samples were produced by mixing the prepolymer and curing agent at a 30 : 1 ratio, respectively. The mixture is hand mixed and degassed in a vacuum chamber for 15 min then poured into the molds described below. Curing occurred at 70 °C for 18 hours. Curing of the Sylgard under this protocol was monitored using shear rheometry as described in the SI to confirm it reaches a terminal shear modulus near ~70 kPa. Samples were removed from the oven and left to cool to room temperature before testing.

Fig. 1 shows the sample designs used in this work. Initial samples were cast into a square petridish and then cut into cruciforms using a Cricut Maker 3 (picture shown in SI). The 'Knife Blade' cutter attachment was used and the Sylgard samples were secured onto an adhesive-backed mat of a standard to strong grip. Fig. 2(a) and (b) shows the CAD image used for the two main specimen geometries used in this study. First is a cruciform shape, inspired by Donne *et al.*,[19] denoted as (CF). The second is a Maltese Cross shape (MC), which have tapered legs (denoted as trapezoid) that end with straight leg segments used for clamping.

Later, samples that required a thicker leg segment (such as MCT and MCTS) were produced through a molding process. The molds were 3D printed with ABS. Sylgard 30 : 1 was mixed, degassed and poured directly into the mold. After following the same curing procedure prescribed, the samples were carefully extracted to avoid corner deformation.

1.2 Methods

1.2.1 Biaxial tension. Biaxial tension measurements were performed on a Cellscale Biotester 5000. Fig. 2(c) shows an image of this setup. The Biotester has four independently controllable actuators that can independently stretch a sample in two perpendicular directions. Displacement rates for the actuators range from 25 μm s^{-1} to 20 mm s^{-1}. Both the x and y

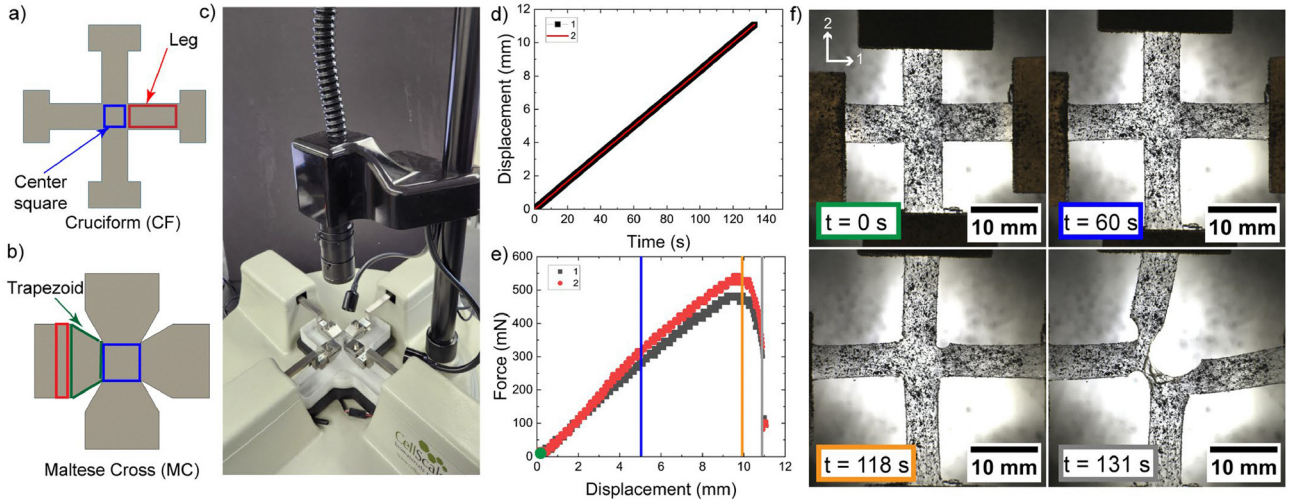

Fig. 2 (a) Schematic of the cruciform (CF). (b) Schematic of Maltese Cross (MC). (c) Image of the Cellscale Biotester 5000 showing four arms ending with clamp grips. The center between the clamps is viewed by a camera which is used for digital image correlation (DIC). (d) Plot of the imposed displacements *vs.* time for a CF sample undergoing equibiaxial extension. (e) Plot of force *vs.* displacement for the same CF sample where marked colors correspond to the time signatures of the images depicted in (f).

directions are equipped with load cells that have a 23 N force capacity. The setup also includes LED lighting and a 2048 pixels by 2048 pixels resolution camera that is used to monitor the sample during testing. The inline actuators on both sides of the sample are both deformed at the same rate so that center of the sample center stays in the camera's field-of-view during testing. As can be seen in Fig. 2(d)–(f), the raw data from this setup includes the x and y displacements, x and y forces, and time synchronized sample images. In addition to the raw images, the control software for the Biotester has built-in digital image correlation (DIC) capabilities and is used for the DIC results presented in this work.

The sample images were gathered at a rate of 5 frames per second during testing. The pixel size is approximately $\sim 20 \times 20$ μm. During the equibiaxial measurements, displacement in both directions was set to 5 mm min^{-1}. During the uniaxial extension measurements on the MCT samples, the x displacement rate was set to a rate of 5 mm min^{-1}. In the y direction, the displacement was set to track zero force. Displacement rates used were kept constant at 5 mm min^{-1} for both uniaxial and biaxial measurements.

Fig. 1(d) shows the displacement–time and force–displacement (F–δ) graphs of a cruciform sample under equibiaxial loading. Images corresponding to the indicated time signatures are shown at four different states of stretch: at t = 0 s (green circle) the clamped CF sample is at rest. At t = 75 s (blue line), the sample is entering nonlinear regime. At t = 130 s (orange line), the image shows the onset of tearing near the y-axis leg. This results in the failure that is observed at t = 133 s (grey line).

1.2.2 Inflation. Samples were also tested on a custom setup designed to perform equibiaxial inflation of thin films. A video of inflation and raw data from this setup are contained in the SI. The setup consists of a syringe pump, custom machined inflation chamber rig, an inline pressure sensor, and a camera to visualize the deformation.

2 Axial compliance of cruciform legs

The deformation of the initial CF sample design (inspired by Donne *et al.*[19]) at increasing displacements is shown in the top row of Fig. 3(a). These images correlate to the displacement–time and force–displacement plots in Fig. 3(b). Upon observing the deformation of this initial sample, several issues arise that hinder the measurement of failure under controlled multiaxial stress states. First, the legs that connect the center square to the clamp stretch significantly more than the center square. While the elastic response of the center square can still be characterized in this sample, failure will be driven by the large deformations in the sample legs. Second, by having legs in two perpendicular directions, a traction will develop at the edge of the center square where the side legs must stretch in the transverse direction to accommodate the applied deformation. This leads to local variations in the deformation that hinder the ability to apply a controlled multiaxial stress state. The final issue is that the corners at the junction of the legs are sharp and will act as stress concentration points. All three of these issues are addressed experimentally below.

As seen in Fig. 3(c), the legs and the center square of a cruciform sample can be modelled as spring elements in series. Using this perspective, the total compliance of the system C_{Tot} is determined by the compliance of the center square C_{c} and twice the compliance of a leg C_{L},

$$C_{\mathrm{Tot}} = C_{\mathrm{c}} + 2C_{\mathrm{L}} = \frac{1}{2ET} + \frac{2l}{wTE}. \quad (1)$$

The derivation of this equation assumes linear elasticity and is contained in the SI. Here, E is Young's Modulus, T is

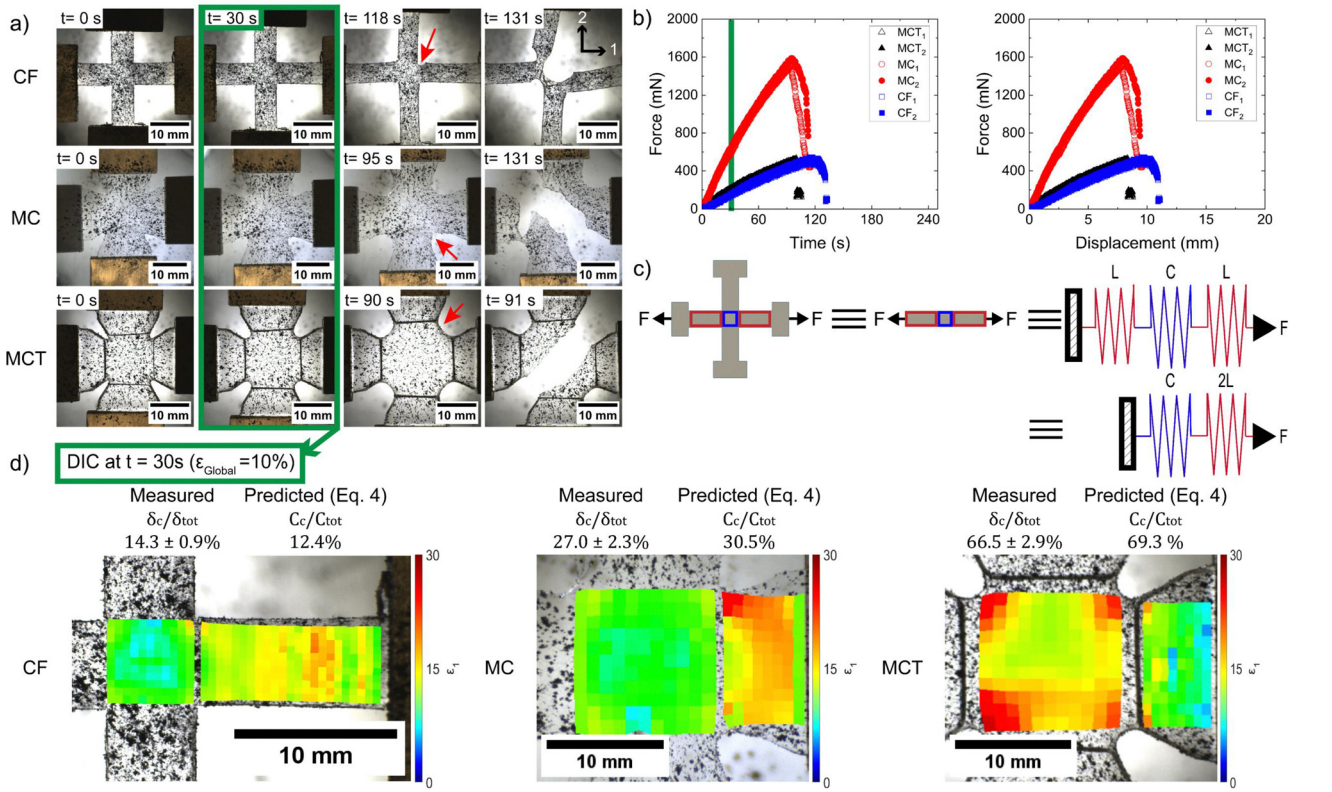

Fig. 3 (a) Progressing images of equibiaxial extension for each of the CF, MC, and MCT (where T stands for thickened legs) samples to failure. (b) Plots of force *vs.* time and force *vs.* displacement for these three geometries. (c) Geometric construction of a spring model showing how the CF geometry is simplified to local regions which are modeled as a set of springs in series. (d) DIC of overlay of local values of ε_1 for each geometry with the measured and predicted relative compliance of the center square at time t = 30 s.

thickness, l is length, and w is width. Eqn (1) can be used to calculate the relative compliance of the center square $\frac{C_c}{C_{Tot}}$ which is predicted to be 12.4%. As seen in Fig. 3(d), this prediction can be compared to the relative displacements in each component using eqn (2).

$$\frac{C_c}{C_{Tot}} = \frac{\delta_c}{\delta_{Tot}} = \frac{\varepsilon_c w_c}{\varepsilon_c w_c + 2\varepsilon_L l_L} = 14.3 \pm 0.9\%, \qquad (2)$$

where DIC is used to quantify the local strains. Although it is assumed in eqn (2) that the strain field is homogeneous, there exists variability depending on the design chosen (see Fig. 3(d)). The analysis is made on the DIC strain grid on a row-by-row basis, where the strains are averaged for each of the center strains and leg strains (ε_c and ε_L), respectively. Then the averaged strains are used to calculate δ_c/δ_{tot} for each row according to eqn (2). Finally, a mean value of δ_c/δ_{tot} and standard deviation are obtained from the distribution of those values. Another method is to use only the center square boundary values. δ_c/δ_{tot} values based on top and bottom rows from the DIC grid are similar to the above method (shown in Table S2).

The agreement between the predicted and measured values suggests that, while this model of the local compliances is simple in construction, it likely identifies the main geometric and materials parameters that can be tuned to control the relative compliance. Notably, as a result of setting the overlap region to be a square, its compliance can only be tuned by changing its thickness and modulus relative to the legs. On the other hand the compliance of the legs can be tuned by altering their length, width, thickness, or modulus. As seen in Fig. 3, the first modification made to the CF samples is to widen and shorten the leg to get the Maltese Cross (MC) samples. An updated spring model can be constructed by adding a term to model the trapezoid region that widens as it approaches the clamp,

$$C_{Tot} = C_c + 2C_T + 2C_L \approx \frac{1}{2ET} + \frac{2l_T}{w_c ET} + \frac{3l_L}{2w_L TE},$$
$$\frac{C_c}{C_{Tot}} = \frac{\delta_c}{\delta_{Tot}} = \frac{\varepsilon_c w_c}{\varepsilon_c w_c + 2\varepsilon_T l_T + 2\varepsilon_L l_L}. \qquad (3)$$

This model predicts a value of $\frac{C_c}{C_{Tot}} = 30.5\%$ which agrees well with the experimentally measured value of 27.0 ± 2.3% using eqn (3) and the method detailed above.

While the relative compliance increases when the legs are shortened and widened, it is still below the value of 50% where the imposed deformation would begin to stretch the center more than the legs. To push towards this regime it is necessary to change either the relative thicknesses or relative moduli of the legs to the center. Altering the modulus requires

the creation of heterogeneous samples with either a different material or altered structure in the legs. This option is set aside due to a desire to keep the molding process as straightforward as possible. Due to this, the leg thickness is increased to get the MCT samples shown in Fig. 1(c). Here, eqn (3) predicts a relative compliance of $\frac{C_c}{C_{Tot}} = 69.3\%$ which is slightly larger than the experimentally measured value of 66.5 ± 2.9% using eqn (3) and the same method detailed above. The slight difference here is likely caused by the model approximation that the strain field is uniform, whereas the DIC overlay in Fig. 3(d) shows that a non-uniform distribution of strains develops.

Importantly, tuning the dimensions of the legs increases the axial compliance ratio up to 66.5 ± 2.9%. Since this value is larger than 50%, this means that the MCT samples have more stretching in the center than in the legs. Moving forward, MCT samples are used because the majority of the deformation occurs in the center where the biaxial stress state develops.

3 Local strain variations in the center

Fig. 4 quantifies the strain distribution that develops in the MCT geometry. Videos of every run in this figure are available

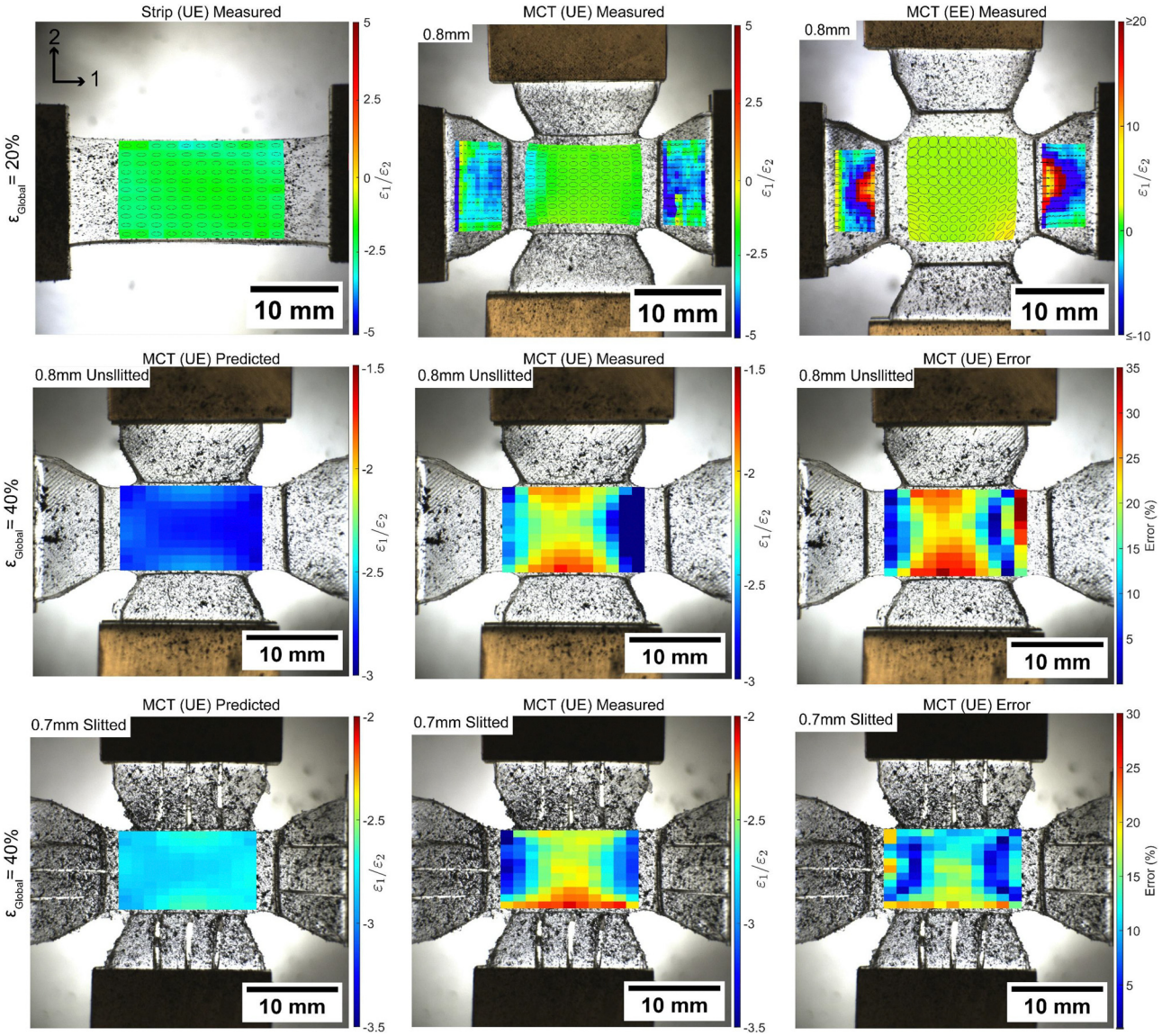

Fig. 4 DIC strain analysis showing the relative strain ratio between the 1 and 2 directions. First row (left to right): measured $\varepsilon_1/\varepsilon_2$ values for a strip in UE, followed by measured $\varepsilon_1/\varepsilon_2$ for MCT geometry in UE, and measured $\varepsilon_1/\varepsilon_2$ for MCT in EE, all at 20% global strain. Second row, MCT sample with no leg cutting extended in UE at 40% global strain values showing (left to right): predicted $\varepsilon_1/\varepsilon_2$, followed by the measured $\varepsilon_1/\varepsilon_2$, followed by the percent magnitude error in reference to the prediction overlaid on top of the same image and time signature. Third row, MCT sample with 3-slices per leg extended in UE at 40% global strain values showing (left to right): predicted $\varepsilon_1/\varepsilon_2$, followed by the measured $\varepsilon_1/\varepsilon_2$, followed by the percent magnitude error in reference to the prediction overlaid on top of the same image and time signature.

as SI Videos. Similarly, plots of the measured force *vs.* displacement profiles are contained in the SI. As a point of comparison, the strain distribution of a strip without side legs subjected to uniaxial extension is shown at 20% global effective strain in the upper left hand corner. Global effective strain is defined as the displacement divided by the initial distance between the clamps and is used as a label to help select images to compare between samples. The global effective strain is not used in any of the calculations presented in this work. The principal strain ratio map of the strip specimen shows a uniformly distributed strain field, where $\varepsilon_1/\varepsilon_2$ is not significantly altered near the sample edge. The image in the center of the top row shows the strain field for an MCT sample subjected to uniaxial extension. Uniaxial extension is applied by setting a constant velocity in the one direction and having the two direction track the zero force point. Unlike the strip, the distribution of strain varies in the center square. More stretching develops at the center of the square than at the edge near the cliff where the leg becomes thicker. This is most likely caused by the traction that develops due to the transverse stretching of the side legs. Similarly, the image in the third column of the first row shows that a non-uniform distribution of strain develops in MCT samples when subjected to equibiaxial extension. In comparing the uniaxial extension and equibiaxial extension MCT samples, it is apparent that a more complex deformation field develops in the legs when deformation that results in transverse leg stretching is applied in the opposite axis.

Using the local deformations quantified by DIC, a prediction of the ratio of $\frac{\varepsilon_1}{\varepsilon_2}$ can be made. In the low strain regime, this ratio is related to the Poisson's ratio of the material. As derived in the SI, this ratio can still be calculated for an incompressible material at large strains as,

$$-\frac{\varepsilon_1}{\varepsilon_2} = 1 + \varepsilon_1 + \sqrt{1+\varepsilon_1}. \tag{4}$$

Eqn (4) is used to calculate the predicted ratio of $\frac{\varepsilon_1}{\varepsilon_2}$ from the DIC values of ε_1 and is overlaid on an MCT sample stretched to a global strain of 40% in the first image of the second row. The image in the second column of the second row shows the values of $\frac{\varepsilon_1}{\varepsilon_2}$ directly quantified by the DIC. By combining these two values, the local errors in the development of a uniaxial extension deformation state are quantified in the last image of the second row. Significant errors up to $\sim$ 35% occur near the edge of the sample where a traction develops due to the transverse stretching of the side legs.

A method of decreasing the transverse stiffness of the leg while not altering the axial compliance is needed to reduce the local errors in the deformation state. One such method is to alter the deformation mode by introducing regularly spaced cuts parallel to the axial direction in the legs. Slicing the legs is aligned with approaches previously implemented in cruciforms for stiff materials.[46,49] Introducing these cuts alters the transverse deformation of the leg from being resisted by a stretching stiffness to being resisted by a beam bending stiffness (see SI for an illustration comparing these two deformation modes in MCT samples). Assuming linear elasticity and a Poisson's ratio $\nu = 0.5$[50] gives the relative stiffness of the beams k_{beam} to the stretching stiffness of the leg in UE k_{UE} as

$$\frac{k_{\text{beam}}}{k_{\text{UE}}} \approx \frac{1}{\frac{n^2}{4} + \frac{9}{10}}, \tag{5}$$

where n is the number of beams (number of cuts plus one). Note that the stiffnesses calculated here are geometry dependent and would have units of N m^{-1}. Eqn (5) predicts that creating four beams reduces the transverse stiffness to a relative value of $\frac{k_{\text{beam}}}{k_{\text{UE}}} = 0.204$ compared to the stretching stiffness. This means that the transverse stiffness should be reduced by a factor of roughly 5 and a more uniform distribution of strains should develop. While there should be a reduction in stiffness, the model developed here does not translate to a quantitative prediction of the local errors. As can be seen in the final row of the Fig. 4 more uniform distribution of strains does develop where the errors are of the order of 15–20% as compared to the $\sim$35% errors observed without slicing the legs. Given this reduction in error, sliced leg samples will be used in the following section.

4 Impact of corner geometry on failure stress

Critical failure stresses were measured on MCT samples and dogbone (DB) samples subjected to uniaxial extension as shown in Fig. 5(a). The stresses are calculated based on the ratio of the force registered by the load cell to the unit unstrained area of the cross section. For the MCT samples, this is taken as the corner-to-corner cross sectional area of the center square. The MCT samples were cast into molds made with corner radii of 0.2, 0.6, 1.0, and 1.4 mm. The critical stress at failure is plotted against the inverse of these radii R^{-1} in Fig. 5(a) and (b) for uniaxial and equibiaxial stretching to failure, respectively. It is evident in Fig. 5(a) that increasing the MCT corner radius does not result in agreement with the critical stress measured in DB samples. After rounding the sharp corners beyond 0.2 mm, further increases in radius have limited effect on failure stress. The failure stresses for all the MCT samples are less than the dogbone samples due to the stress concentration that develops at the corner in the MCT geometry.

Similarly, failure stresses measured with MCT samples and inflation samples in equibiaxial extension are shown in Fig. 5(b). Inflation is used as a control because an inflated sheet will be subjected to an equibiaxial extension during pressurization. Inflation is performed by pressurizing a clamped sheet through a circular orifice (see SI for details).

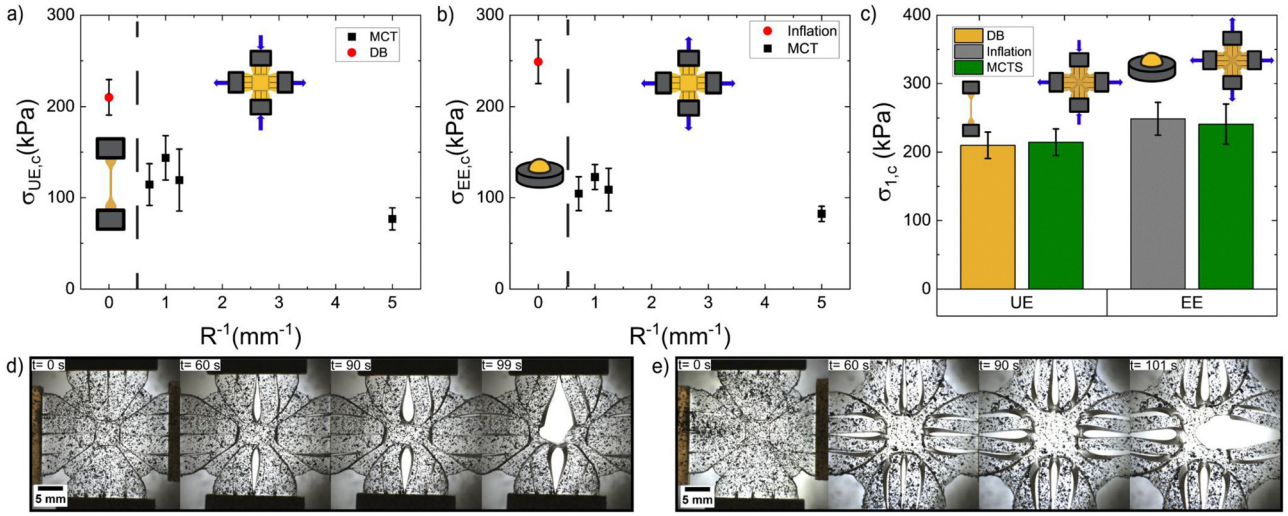

Fig. 5 Influence of corner geometry on the critical stress in the 1 direction $\sigma_{1,c}$ in uniaxial and biaxial measurements. (a) MCT design of different corner radii in UE against control in the form of dogbone (DB) samples. (b) MCT design of different radii in EE against equibiaxial inflation. The horizontal axis shows the inverse of the corner radius R^{-1} of the MCT specimen. (c) the redesigned corner geometry (MCTS) against DB in UE and inflation in EE, showing agreement in the critical stresses. (d) Sequence of MCTS in UE from rest to failure. (e) Sequence of MCTS in EE from rest to failure. Measurements were taken at 5 mm min^{-1} extension. Inflation samples were pressurized at a rate of 100 ml min^{-1}.

Max inflation stresses are calculated using,

$$\sigma_c = \frac{1}{2}\frac{P_{max}R}{T_0}, \quad (6)$$

where R is the instantaneous radius of the inflated bubble and T_0 is the initial film thickness. Increasing corner radius results in a modest increase in the observed MCT failure stresses. However, all MCT failure stresses are approximately half of those observed in the inflation samples. This difference indicates that altering the corner radius does not mitigate failure due to high corner stretching relative to the center square (see Fig. S6).

Since rounding off the corner radius for MCT samples does not result in failure stresses comparable to those from the independent measurements, further modification of the geometry is necessary. Two additional changes are implemented in the final geometry with the goal of reducing the influence of the free edge at the corner. First, the thick tapered region is extended further into the sample. This alteration enables the second change which consists of adding thin material connecting each tapered region. This pushes the free edge away from the corner. These changes make the slices introduced into the legs critical to the sample design. The slicing of the legs to the edge of the thick tapered region defines the boundary of the center square and ensures that a central plane exists in each direction where the minimum width is that of the center square. This final geometry is named the maltese cross thickened leg stress-distributed sample or MCTS sample for short. As seen in Fig. 5(c), the failure stresses measured in MCTS samples are comparable to both of the independent measurements in uniaxial extension and equibiaxial extension. As can be seen in the images of Fig. 5(d) and (e), the failure initiation shifts under each loading to occur not at the free edge around the corner, but at the center plane of the sample where the slice defines the boundary of the center square. This shows that MCTS samples effectively mitigate the corner stress concentrations observed in the MCT samples.

While the results presented above demonstrate the potential of using MCTS samples to measure failure stresses, it is important to discuss the limitations of these findings. One limitation is the complexity of the MCTS cruciform geometry relative to other designs such as the MC geometry. The MCTS geometry is specifically designed to measure failure stress while simpler designs similar to the MC geometry exist and have been demonstrated to be useful in measuring the relationship between stress and strain.[51] Another limitation is that the agreement between the failure stresses in control measurements and MCTS samples of the silicone elastomer presented above may not transfer to materials with more complicated large strain constitutive behavior. For example, a material such as natural rubber that undergoes strain-induced crystallization may have interesting tradeoffs in terms of the relative compliance of the center square to the legs. Despite these limitations, the MCTS geometry is still attractive for quantifying the biaxial failure stresses of soft elastomers.

5 Conclusions

This work demonstrated that the failure stress of non-strain crystallizing soft elastomers exposed to controlled biaxial stress states can be characterized with MCTS cruciform samples. Accomplishing this required careful control of the axial compliance of the leg, the transverse compliance of the leg, and corner geometry. Controlling all three of these parameters resulted in the development of sliced MCTS samples. These findings provide a means through which the failure surface of

soft elastomers can be rigorously quantified. Doing so will advance our understanding of the nonlinear behavior of soft solids during phenomena such as cavitation and yielding. Although MCTS samples can be used to apply controlled biaxial stress states, this technique is unable to subject samples to compressive stresses. Developing methods to apply controlled compressive stresses to the point of failure in soft materials presents an opportunity for future researchers.

Conflicts of interest

The authors declare no conflicts of interest.

Data availability

The data supporting this article is included in the SI. The SI contains the list of supplementary video files, summary tables of the data measured, further experimental details, and the derivations of equations used in the main text. See DOI: **https://doi.org/10.1039/d5sm00644a**.

Acknowledgements

This work was funded through startup funds from the University of Akron.

References

1 W. Whitney and R. D. Andrews, *J. Polym. Sci., Part C: Polym. Symp.*, 1967, **16**, 2981–2990.
2 D. C. Drucker, *Metall. Trans.*, 1972, **4**, 667–673.
3 M. Maitra, K. Majumdar and A. Das, *AIAA J.*, 1973, **11**, 1428–1429.
4 R. Raghava, R. M. Caddell and G. S. Y. Yeh, *The macroscopic yield behaviour of polymers*, 1973.
5 R. J. Oxborough and P. B. Bowden, *Philos. Mag.*, 1974, **30**, 171–184.
6 J. A. Sauer, *Polym. Eng. Sci.*, 1977, **17**, 150–164.
7 M. H. Yu, *Appl. Mech. Rev.*, 2002, **55**, 169–218.
8 I. M. Ward and J. Sweeney, *Mechanical properties of solid polymers*, Wiley, 2013, p. 461.
9 W. Nöhring, F. Conrad, V. Giannella, G. Dhondt, C. Kontermann, R. Citarella and M. Oechsner, *Eng. Fract. Mech.*, 2025, **325**, 111296.
10 V. Giannella, G. Dhondt, C. Kontermann and R. Citarella, *Int. J. Fatigue*, 2019, **123**, 296–307.
11 S. P. Danielsen, H. K. Beech, S. Wang, B. M. El-Zaatari, X. Wang, L. Sapir, T. Ouchi, Z. Wang, P. N. Johnson, Y. Hu, D. J. Lundberg, G. Stoychev, S. L. Craig, J. A. Johnson, J. A. Kalow, B. D. Olsen and M. Rubinstein, *Chem. Rev.*, 2021, **121**, 5042–5092.
12 X. Zhao, X. Chen, H. Yuk, S. Lin, X. Liu and G. Parada, *Chem. Rev.*, 2021, **121**, 4309–4372.
13 A. C. Ugural, *Stresses in Beams, Plates and Shells*, CRC Press, 3rd edn, 2009, pp. 1–596.
14 S. S. Sternstein and F. A. Myers, *J. Macromol. Sci., Part B: Phys.*, 1973, **8**, 539–571.
15 R. V. Mises, *Nachr. Ges. Wiss. Goettingen, Math.-Phys. Kl.*, 1913, **4**, 582–592.
16 J. de Saint-Venant, *J. Pure Appl. Math.*, 1871, **16**, 308–316.
17 M. Rankine, *Philos. Trans. R. Soc. Londony*, 1857, **147**, 9–27.
18 H. Tresca, *Mémoire sur l'écoulement des corps solides soumis á de fortes pressions*, Gauthier-Villars, 1864.
19 C. D. Donne, K.-H. Trautmann and H. Amstutz, *"Cruciform Specimens for In-Plane Biaxial Fracture, Deformation, and Fatigue Testing", Multiaxial Fatigue and Deformation: Testing and Prediction, ASTM STP 1387*, ed. S. Kalluri and P. J. Bonacuse, 2000, DOI: **10.1520/STP13517S**.
20 T. Kawamura, K. Urayama and S. Kohjiya, *J. Soc. Rheol.*, 2003, **31**, 213–217.
21 A. Avanzini and D. Battini, *Adv. Mater. Sci. Eng.*, 2016, **2016**, 1–12.
22 J. J. Hu, G. W. Chen, Y. C. Liu and S. S. Hsu, *Exp. Mech.*, 2014, **54**, 615–631.
23 Y. M. Luo, T. T. Nguyen, H. Attar, L. Chevalier and F. Lesueur, *Polym. Test.*, 2022, **113**, 1–12.
24 S. Hartmann, R. R. Gilbert and C. Sguazzo, *GAMM Mitt*, 2018, **41**, 1–14.
25 L. M. Palacios-Pineda, I. A. Perales-Martínez, M. R. Moreno-Guerra and A. Elías-Zúñiga, *Nanomaterials*, 2017, **7**, 1–13.
26 X. Zhao, Z. C. Berwick, J. F. Krieger, H. Chen, S. Chambers and G. S. Kassab, *Exp. Mech.*, 2014, **54**, 343–356.
27 A. Makinde, L. Thibodeau and K. W. Neale, *Exp. Mech.*, 1992, **32**, 138–144.
28 S. Demmerle and J. P. Boehler, *J. Mech. Phys. Solids*, 1993, **41**, 143–181.
29 S. D. Waldman and J. M. Lee, *J. Mater. Sci.: Mater. Med.*, 2002, **13**, 933–938.
30 A. Makris, T. Vandenbergh, C. Ramault, D. V. Hemelrijck, E. Lamkanfi and W. V. Paepegem, *Polym. Test.*, 2010, **29**, 216–223.
31 B. Yohsuke, K. Urayama, T. Takigawa and K. Ito, *Soft Matter*, 2011, **7**, 2632.
32 M. Johlitz and S. Diebels, *Arch. Appl. Mech.*, 2011, **81**, 1333–1349.
33 T. Katashima, K. Urayama, U. il Chung and T. Sakai, *Soft Matter*, 2012, **8**, 8217.
34 X. Zhao, *Soft Matter*, 2014, **10**, 672–687.
35 Y. Kondo, K. Urayama, M. Kidowaki, K. Mayumi, T. Takigawa and K. Ito, *J. Chem. Phys.*, 2014, **141**, 134906.
36 M. Fujikawa, N. Maeda, J. Yamabe, Y. Kodama and M. Koishi, *Exp. Mech.*, 2014, **54**, 1639–1649.
37 E. Lamkanfi, W. V. Paepegem and J. Degrieck, *Polym. Test.*, 2015, **41**, 7–16.
38 T. T. Mai, T. Matsuda, T. Nakajima, J. P. Gong and K. Urayama, *Macromolecules*, 2018, **51**, 5245–5257.
39 T.-T. Mai, T. Matsuda, T. Nakajima, J. P. Gong and K. Urayama, *Soft Matter*, 2019, **15**(18), 3719–3722.
40 K. Morris, A. Rosenkranz, H. Seibert, L. Ringel, S. Diebels and F. E. Talke, *J. Appl. Polym. Sci.*, 2020, 1–9.
41 M. Jiang, R. L. Sridhar, A. B. Robbins, A. D. Freed and M. R. Moreno, *J. Mech. Behav. Biomed. Mater.*, 2021, **114**, 1–21.

42 T. Aoyama, N. Yamada and K. Urayama, *Macromolecules*, 2021, **54**, 2353–2365.
43 Y. Kodaira, T. Miura, Y. Takano and A. Yonezu, *Polym. Test.*, 2022, **106**, 1–8.
44 D. Pearce, M. Nemcek and C. Witzenburg, *Curr. Protoc.*, 2022, **2**, 1–23.
45 V. Gupta, S. Gupta and A. Chanda, *Biomed. Phys. Eng. Express*, 2023, **9**, 1–11.
46 V. Giannella, D. Amato and M. Perrella, *Eng. Fract. Mech.*, 2022, **261**, 108247.
47 E. Breedlove, C. Chen, D. Lindeman and O. Lopez-Pamies, *J. Mech. Phys. Solids*, 2024, 105678.
48 T. Matsuda, T. Nakajima, Y. Fukuda, W. Hong, T. Sakai, T. Kurokawa, U. I. Chung and J. P. Gong, *Macromolecules*, 2016, **49**, 1865–1872.
49 C. H. Wolf, S. Henkel, A. Burgold, Y. Qiu, M. Kuna and H. Biermann, *Int. J. Fatigue*, 2019, **124**, 595–617.
50 C. W. Barney, M. E. Helgeson and M. T. Valentine, *Extreme Mech. Lett.*, 2022, **52**, 101616.
51 G. Vitucci, *Exp. Mech.*, 2024, **64**, 539–550.